

Creep mechanisms and microstructure evolution of Nextel™ 610 fiber in air and steam[☆]

R.S. Hay^{a,*}, C.J. Armani^b, M.B. Ruggles-Wrenn^b, G.E. Fair^a

^a Air Force Research Laboratory, Materials and Manufacturing Directorate, Wright-Patterson Air Force Base, OH 45433-7817, United States

^b Air Force Institute of Technology, Wright-Patterson Air Force Base, OH 45433-7765, United States

Received 6 November 2013; received in revised form 9 January 2014; accepted 16 January 2014

Available online 5 March 2014

Abstract

Creep rates of Nextel™ 610 alumina fibers were measured at 1100 °C and 100–500 MPa in air and steam. Steam increased creep rates and reduced fiber lifetimes. Fiber microstructures were characterized by TEM. The small amounts of grain growth, fiber-axis grain elongation, and pore growth that occur during creep were quantified. To separate the effects of stress and temperature on microstructural evolution, grain growth and elongation were also quantified for fibers heat-treated for 1–100 h in air at 1100–1500 °C. Grain growth laws were determined. The contributions of pore growth and grain elongation to creep strain were quantified. Grain elongation accounts for a large fraction of the strain during creep in air, but little in steam. Pore growth was more pronounced in steam, but does not create significant creep strain. Creep and failure mechanisms consistent with the observed microstructural changes are discussed.

Published by Elsevier Ltd.

Keywords: Creep; Fibers; Alumina; Steam; Microstructure

1. Introduction

Oxide–oxide ceramic matrix composites (CMCs) are damage tolerant and oxidation resistant, and have good high-temperature mechanical properties in air.^{1–10} They are attractive in comparison to SiC–SiC CMCs when low tensile and interlaminar stress, long times in oxidizing environments at <1200 °C, low thermal conductivity, and low cost drive material selection. Creep rates can be temperature and/or stress limiting for CMCs,^{11,12} particularly for oxide–oxide CMCs. Fiber creep almost always governs creep of CMCs in tension. CMC applications often involve exposure to water, either as a combustion product or as atmospheric humidity. Tensile creep rates of oxide–oxide CMCs with Nextel™ 610 or Nextel™ 720 fibers can be more than an order of magnitude higher in steam than in air.^{13–22} Recently, an order of magnitude enhancement of creep by steam was observed for Nextel™

610 and Nextel™ 720 fibers alone.^{23–25} The mechanisms that promote higher creep rates in steam are therefore of great interest, both for modeling CMC mechanical behavior and for developing new materials systems that are more creep resistant.

Many studies of tensile creep of various alumina-based fibers in air have been conducted,^{26–34} and a lot of research has been done on compressive creep of polycrystalline alumina, with and without various impurities, in air.^{35–48} Most of the work up to 2003 has been thoroughly reviewed.⁴⁷ Only a few studies have been done in environments containing water.^{49–51} These studies report higher creep rates in steam than in air, which is sometimes referred to as hydrolytic weakening. In silicate minerals hydrolytic weakening is well known, and mechanisms involving climb-controlled dislocation creep or enhancement of diffusion-creep have been proposed.⁵²

Creep measurements on polycrystalline alumina fibers usually differ from those on bulk polycrystalline alumina in several ways. Fiber measurements are typically done in tension, while bulk studies are in compression. Fiber grain sizes are usually less than 0.1 μm,^{25,53,54} but bulk polycrystalline grain sizes are usually greater than 1 μm. Fiber diameters are less than 15 μm, so equilibration with the test environment at relatively low temperatures can be achieved faster than in bulk material.

[☆] The views expressed are those of the authors and do not reflect the official policy or position of the United States Air Force, Department of Defense or the U.S. Government.

* Corresponding author. Tel.: +1 937 255 9825; fax: +1 937 656 4296.
E-mail address: Randall.Hay@wpafb.af.mil (R.S. Hay).

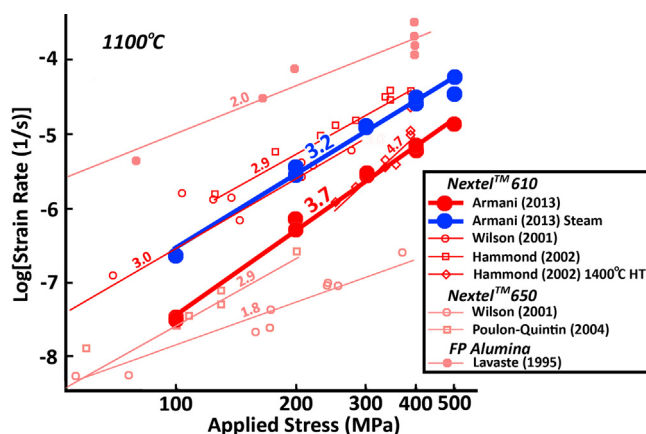


Fig. 1. Steady-state strain rate vs. applied stress of Nextel™ 610 fibers in air and steam. Other alumina fibers are included for comparison.

Nextel™ 610 is a high-purity alumina fiber (>99% Al_2O_3) manufactured by 3M™ Corporation (Minneapolis, MN). The fiber tow contains 400 filaments with an average filament diameter of 12 μm . Trace Fe and Si are added for α -alumina nucleation and grain growth suppression, respectively. Fiber properties, microstructure, and composition were reported elsewhere.^{28,33,54–56} In previous on Nextel™ 610, creep tests were done at 1100 °C in air and in steam for stresses from 100 to 500 MPa.^{23,24} The creep rates in steam were nearly one order of magnitude higher than those in air, and creep lifetimes were lower than those in air (Fig. 1). Flow stress exponents of $n \approx 3.2$ and 3.7 were found in air and in steam, respectively. Tensile strengths were lower at higher loading rates in steam, suggesting operation of an environmentally assisted subcritical

crack growth mechanism. The experiments, creep rates, and microstructural parameters are listed in Table 1.

The previous study of the effects of steam on creep of Nextel™ 610 fiber tows is expanded to include extensive TEM characterization and quantification of microstructure evolution during creep.^{23,24} Small amounts of grain growth, fiber-axis grain elongation, and pore growth are quantified. Some microstructural changes are subtle and require a large amount of data for quantification. To separate the effects of temperature and stress on microstructure evolution, grain growth and fiber-axis grain elongation are also characterized and quantified after heat-treatment under no load, without creep. Creep mechanisms consistent with creep test data and microstructural evolution are discussed. Creep rates in air were lower than those reported elsewhere (Fig. 1).^{33,34} Possible reasons for these differences are discussed. A detailed description of fiber microstructure evolution in air with heat-treatment between 1100 °C and 1500 °C will be published in a forthcoming paper.

2. Experiments

Detailed descriptions of the tensile creep test apparatus and methods used for Nextel™ 610 in air and steam have previously been published.^{23,24} All tests were performed at 1100 °C with a 1 °C/s heat-up rate and a 45 min hold prior to testing. A fiber tow area of $4.52 \times 10^{-8} \text{ m}^2$ was used to calculate engineering stress for the 400 filament tows. Strain was calculated from the specimen elongation measurements using published methods.^{57–59} The cold grip method was used, so fiber elongation was measured outside the furnace. The total fiber elongation was the sum of contributions from different temperature zones: the hot zone with a uniform temperature of 1100 °C, the temperature gradient

Table 1
Summary of creep-rupture results for Nextel™ 610 fiber tows at 1100 °C in laboratory air and in steam.

Environment	Creep stress (MPa)	Creep strain – ϵ (%)	Steady-state creep rate (10^{-8} s^{-1})	Time to rupture (h)	$\log[X \pm \delta]$ (nm)]	$\log[\text{pore diameter} \pm \text{SD}]$ (nm)]	Pore volume (%)	Grain elongation: $\epsilon - \epsilon_0$ (%)	Grain elongation ϵ_C (%)
As received	δ	δ	δ	δ	1.87 ± 0.15	1.06 ± 0.25	2.1	12	δ
Air	100	1.8 ^a	3.6	>100	1.91 ± 0.17	1.05 ± 0.21	1.1	19	6
Air	100	1.5 ^a	3.2	>100	1.91 ± 0.15	0.99 ± 0.27	1.5	13	2
Air	200	16.9	54.5	48.90	1.93 ± 0.17	1.05 ± 0.29	2.6	31	17
Air	200	14.2	74.2	31.60	1.89 ± 0.17	1.12 ± 0.26	3.1	17	8
Air	300	10.8	296.0	6.67	1.91 ± 0.15	1.05 ± 0.27	2.1	20	7
Air	300	7.9	318.0	4.08	1.89 ± 0.16	1.07 ± 0.26	2.2	21	9
Air	400	5.0	739.0	1.30	1.87 ± 0.16	1.05 ± 0.26	2.2	21	13
Air	400	4.2	643.0	1.33	1.88 ± 0.15	1.10 ± 0.26	2.9	16	6
Air	500	4.4	1430.0	0.55	–	–	–	–	–
Air	500	3.0	1400.0	0.42	–	–	–	–	–
Steam	100	9.9 ^a	22.3	>100	1.96 ± 0.14	1.04 ± 0.29	3.8	20	5
Steam	200	15.1	363.0	6.70	1.91 ± 0.16	1.11 ± 0.33	4.8	17	5
Steam	200	14.9	285.0	8.52	1.96 ± 0.15	1.13 ± 0.28	2.9	19	3
Steam	300	6.5	1330.0	0.92	1.91 ± 0.14	1.11 ± 0.24	2.1	7	-5
Steam	300	6.8	1240.0	0.95	1.91 ± 0.14	1.12 ± 0.25	3.3	14	3
Steam	400	3.8	3090.0	0.25	1.90 ± 0.13	1.11 ± 0.26	3.1	13	2
Steam	400	2.1	2480.0	0.20	1.85 ± 0.12	1.03 ± 0.28	2.4	7	1
Steam	500	3.2	5800.0	0.10	1.88 ± 0.14	1.15 ± 0.25	3.5	8	1
Steam	500	3.9	3400.0	0.23	1.90 ± 0.14	1.00 ± 0.28	3.1	17	2

^a Run-out, defined as 100 h at creep stress. Failure of specimen did not occur when the test was terminated.

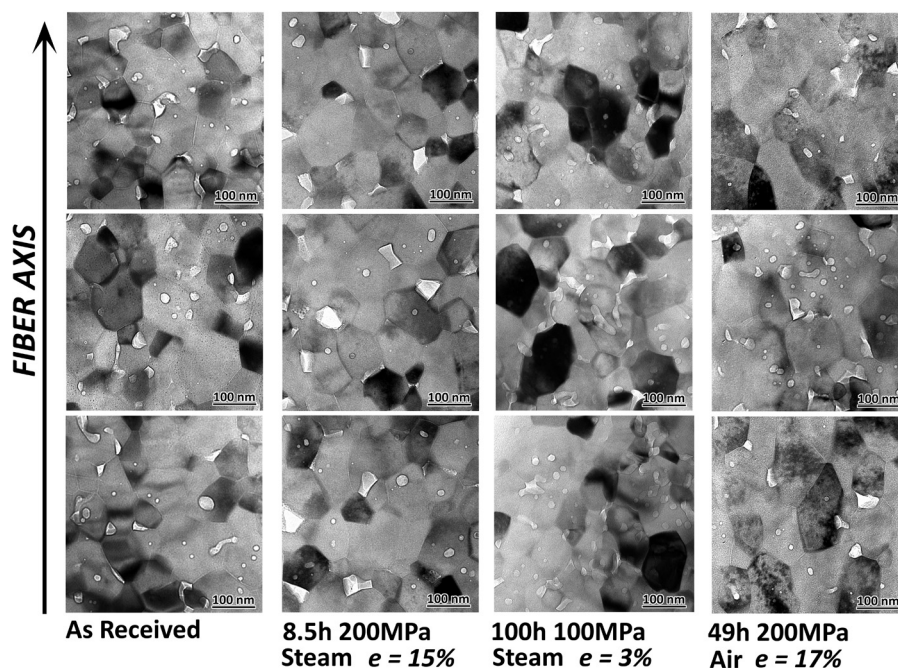


Fig. 2. TEM micrographs of Nextel™ 610 microstructure after creep in air and steam at 1100 °C.

zone, and the cold zone. Furnace temperature profiles were used to determine the effective gauge lengths of 6.64 mm at 1100 °C in air and 5.78 mm at 1100 °C in steam, which were then used to calculate creep strain and strain rate in the hot zone.

To separate effects of creep from those of heat-treatment on fiber microstructure, Nextel™ 610 fiber tows were heat-treated in dry air using an alumina holder and a furnace tube that had previously been baked-out to 1600 °C to vaporize contaminants in commercial alumina.⁶⁰ Heat-treatments were done for 1, 10, and 100 h at 1100 °C, 1200 °C, 1300 °C, 1400 °C, and 1500 °C.

Microstructures of the tested fibers were characterized by TEM (200 kV Phillips CM-200 LaB₆-filament, and 300 kV FEI Titan). Longitudinal TEM sections of tested fibers were prepared by published methods.^{61,62} TEM samples were ion-milled at 5 kV. For high resolution TEM observations in the FEI Titan, 5 kV ion-milling was followed by 1/2 an hour at 1 kV. A total of 30–60 micrographs were taken of at least five filaments from each sample. Grain size distributions and aspect ratios, pore-size distributions, and grain elongation along the fiber axis were quantified using image analysis with Adobe Photoshop™

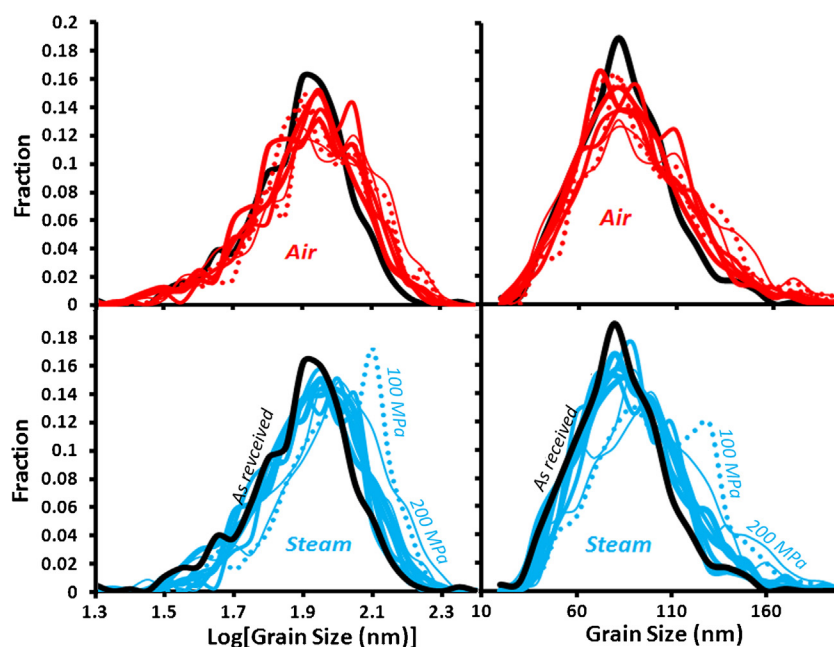


Fig. 3. Log-normal and normal distributions of Nextel™ 610 grain size after creep in air and steam at 1100 °C.

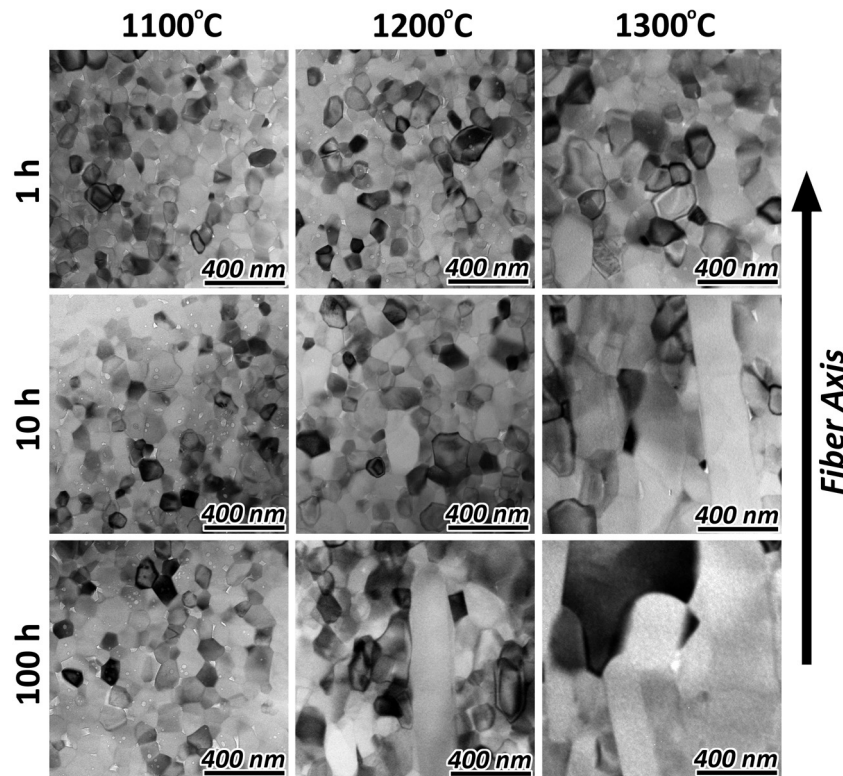


Fig. 4. TEM micrographs of Nextel™ 610 microstructure after heat-treatment in air for 1, 10, and 100 h at 1100 °C, 1200 °C, and 1300 °C.

and Fovea Pro™ software. Grains and pores were identified in digital micrographs by outlining and coloring them black. Contiguous grains were used wherever possible to insure random sampling. The distributions were usually measured for at least 1000 grains or pores in a total of at least five filaments.

Small changes in grain size are resolved by these methods, and trends are clear, but there was still significant scatter. We suspect this is at least in part due to subtle local variations in grain size along and between filaments. Very rarely, small areas with $\sim 2\times$ larger grain size were found. We speculate that more subtle local variation is prevalent. The factor limiting measurement accuracy is therefore the number of filaments sampled, and not the total number of grains, but a large increase in the number of filaments sampled was not feasible in this study.

3. Results and discussion

3.1. Grain growth

TEM micrographs of the Nextel™ 610 fiber as-received, after two different creep experiments in steam, and after one in air, are shown in Fig. 2. Dislocations or subgrain boundaries were difficult to find,²⁴ which was not surprising for the fine-grained microstructures. Three micrographs from three different filaments are shown for each experiment. The experiments in the figure are those with the most creep strain in steam (15%), the longest exposure to steam (100 h), and the most creep strain in air (17%) (Table 1). The fiber axis orientation is vertical.

Microstructure differences are too subtle to easily discern from the micrographs, but differences were apparent after measurements were made for large numbers of grains. This will be discussed in detail.

Grain size distributions for the creep experiments in Table 1 are plotted in Fig. 3. The equivalent grain diameter for non-spherical grains is used in the distributions. Log-normal and normal distributions are both plotted; log-normal are slightly skewed to large grain size and normal to small grain size. The most grain growth was in the fibers exposed to steam for the longest times. These were the creep experiments done at the lowest stresses, 100 and 200 MPa (Table 1). Distributions for the 100

Table 2
Summary of grain growth measurements for Nextel™ 610.

t (h)	1	10	100
$T(^{\circ}\text{C})$	Log[equivalent diameter (nm)]		
1100	1.87 ± 0.16	1.90 ± 0.16	1.88 ± 0.18
1200	1.86 ± 0.18	1.94 ± 0.18	2.06 ± 0.18
1300	2.09 ± 0.18	2.18 ± 0.22	2.39 ± 0.25
1400	2.32 ± 0.23	2.43 ± 0.23	2.58 ± 0.25
1500	2.53 ± 0.26	2.74 ± 0.30	3.00 ± 0.32
$T(^{\circ}\text{C})$	Log[long axis (nm)]		
1100	1.98 ± 0.16	2.01 ± 0.16	1.99 ± 0.18
1200	1.98 ± 0.18	2.05 ± 0.17	2.18 ± 0.19
1300	2.20 ± 0.18	2.32 ± 0.24	2.56 ± 0.29
1400	2.48 ± 0.29	2.60 ± 0.29	2.78 ± 0.31
1500	2.73 ± 0.31	2.96 ± 0.37	3.21 ± 0.38

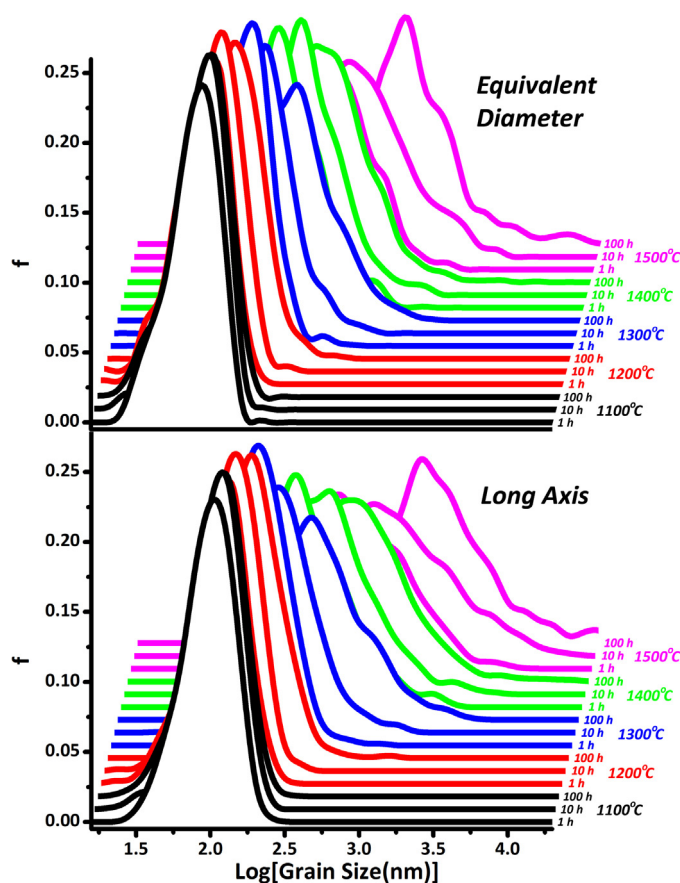


Fig. 5. Log-normal distributions of Nextel™ 610 grain size after heat-treatment in air at 1100–1500° for 1–100 h. Distributions for equivalent grain diameter and the long grain axis are both shown.

and 200 MPa creep tests in steam, with microstructures shown in Fig. 2, are identified in Fig. 3 and denoted by dashed and thin lines, respectively. Grain size distributions for as-received fiber are shown in black for comparison. The log[average] (X)

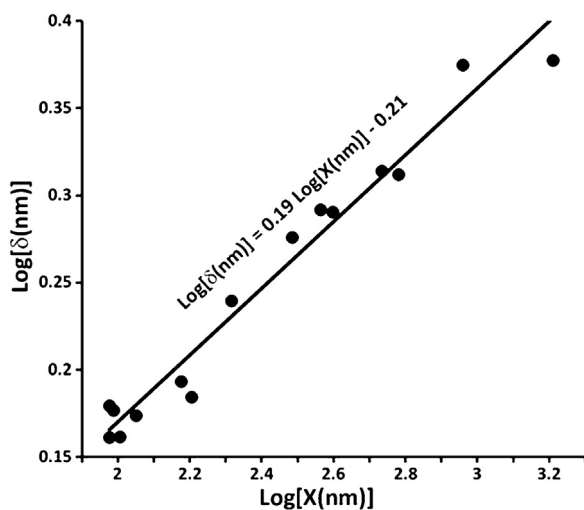


Fig. 6. The relationship between the log-normal standard deviation (δ) and average grain size (equivalent diameter) (X) for Nextel™ 610 after heat-treatment in air at 1100–1500° for 1–100 h.

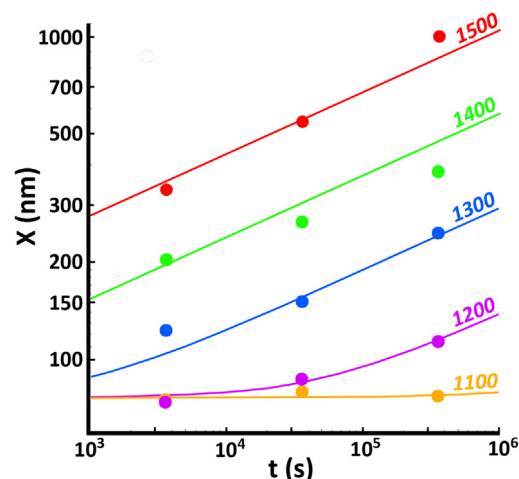


Fig. 7. X for Nextel™ 610 (equivalent diameter) after heat-treatment in air at 1100–1500° for 1–100 h. The best fit to the grain growth law (2)–(3) is shown.

and log[standard deviation] (δ) for equivalent grain diameter are listed in Table 1.

TEM micrographs of as Nextel™ 610 fiber heat-treated for 1, 10, and 100 h at 1100 °C, 1200 °C, and 1300 °C are shown in Fig. 4. The scale and fiber-axis are the same for all micrographs. The large grain sizes that developed during heat-treatment at 1400 °C and 1500 °C cannot be illustrated at the same scale, so they are not included in the figure. Gradual development of plate-like grains with the long grain axis oriented along the fiber axis is evident for 10 and 100 h heat-treatments at 1200° and 1, 10 and 100 h at 1300 °C. At lower temperatures and shorter times grain morphology is subjectively equant. The c-axis (hexagonal cell), or [1 1 1] axis for the primitive rhombohedral alumina cell is normal to the plate surface and perpendicular to the fiber axis. A small fraction of plate-like grains are relatively large in size, and suggest incipient abnormal grain growth. Abnormal grain growth for plate-like grains is well known for α -alumina,

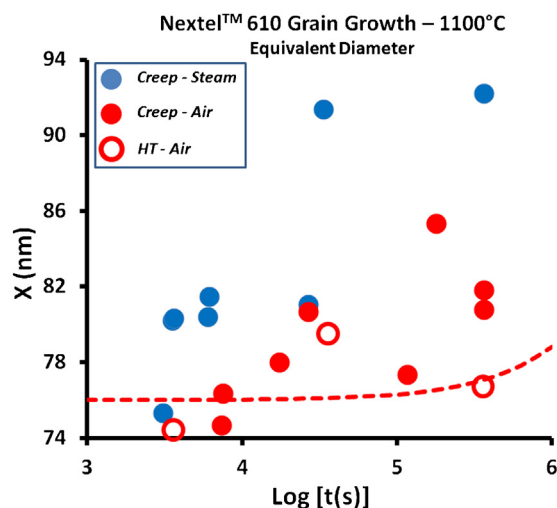


Fig. 8. X for Nextel™ 610 (equivalent diameter) after creep experiments in steam and air at 1100 °C. The best fit to the grain growth law (2)–(3) at 1100 °C is shown as a dashed line. X for fibers heat-treated in air, without creep, are shown as open circles.

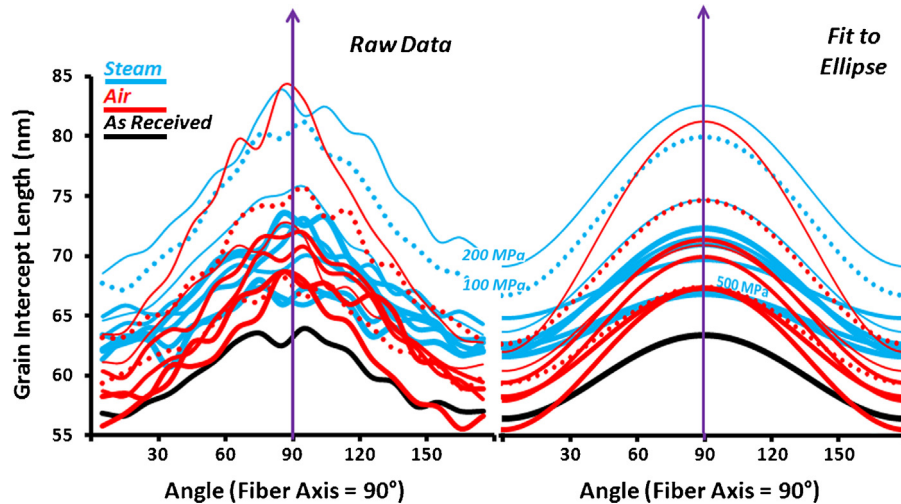


Fig. 9. Grain intercept lengths for 1100 °C creep-tested (Table 1) and as-received Nextel™ 610 fibers along lines with different orientations from the fiber-axis. Lines along the fiber axis are at 90°. The raw data (left) and best fit to an ellipse (right) are shown.

and is related to concentrations of impurities such as Si, Fe, Ca, Mg, and Ti, and the chemistry of intergranular films or “complexions”.^{63–70} Most of these studies involve higher temperatures with grain growth starting from grain sizes at least an order of magnitude larger than those found in Nextel™ 610. However, abnormal growth of plate-like grains, in this case associated with the depletion of intergranular Si, has been previously reported for Nextel™ 610.^{63,70}

Log-normal grain size distributions for equivalent grain diameter and the long grain axis are shown in Fig. 5 for all experiments from 1100 °C to 1500 °C, and the log[average] (\bar{X}) and log[standard deviation] (δ) for equivalent grain diameter are listed in Table 2. Normal distributions were also plotted, but these were highly asymmetric for distributions with larger average grain size. These distributions are reasonably symmetric over the entire time and temperature range, but the log[standard deviation] (δ) clearly increases with \bar{X} (Fig. 6). The distributions are therefore not self-similar, and normal grain growth, by itself, does not describe grain growth kinetics.⁷¹ However, the change in δ is gradual with \bar{X} (Fig. 6), and can be described by a simple relationship:

$$\log[\delta(\text{nm})] = 0.19 \log[\bar{X}(\text{nm})] - 0.21 \quad (1)$$

This suggests a gradual, rather than abrupt, change from normal to abnormal grain growth, or to some other grain growth mechanism, that is spread out over the entire grain size range. It therefore makes little sense to try and distinguish separate regions of normal and abnormal grain growth; the kinetics are calculated for what is assumed to be combined growth mechanisms throughout the grain size ranges from 1100 °C to 1500 °C.

The log-normal distributions best represent grain size distributions in the heat-treated fibers, as is typical for grain growth studies,⁷² including alumina.⁷¹ To distinguish between effects of heat-treatment and stress, these distributions were also used for the creep tested fibers. Since grain morphology in the creep tested fibers was subjectively equant, we use the equivalent grain diameter (\bar{X}) for comparison. Stereological corrections were

not applied to grain size distributions. A correction factor of $\sim 2/\sqrt{3}$ applies to equant grains, but application of this factor is problematic for anisotropic grain shapes. These assumptions are clearly crude approximations after extensive grain growth and formation of plate-like grains occurs, but are assumed to be sufficient to distinguish between effects of heat-treatment and stress on grain growth at 1100 °C, where grain morphology is nearly equant. A thorough quantification of microstructure evolution in Nextel™ 610 that accounts for grain shape anisotropy, grain orientation, and stereological factors will be presented in a forthcoming paper.

Grain growth kinetics were calculated using the usual expression^{71,72}:

$$\bar{X}^m - \bar{X}_0^m = Kt \exp\left(\frac{-Q}{RT}\right) \quad (2)$$

where \bar{X}_0 is the initial average grain size from a log-normal distribution, m is a growth exponent, K is a rate constant, t is

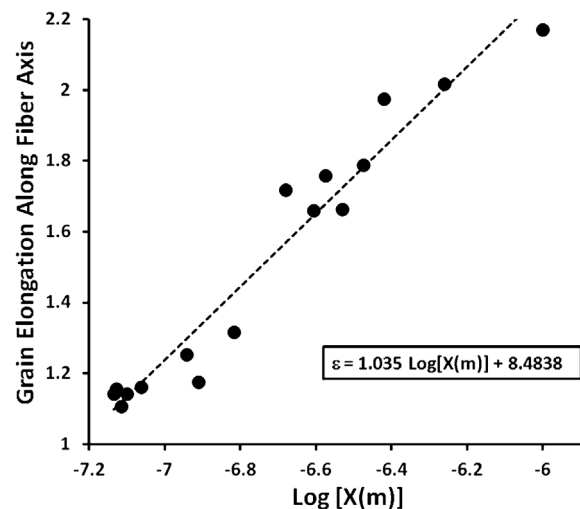


Fig. 10. Grain growth along fiber axis ($1 + \epsilon_{GG}$) vs. $\log[\bar{X}(\text{nm})]$ for Nextel™ 610 fibers heat-treated in air for 1–100 h at 1100–1500 °C.

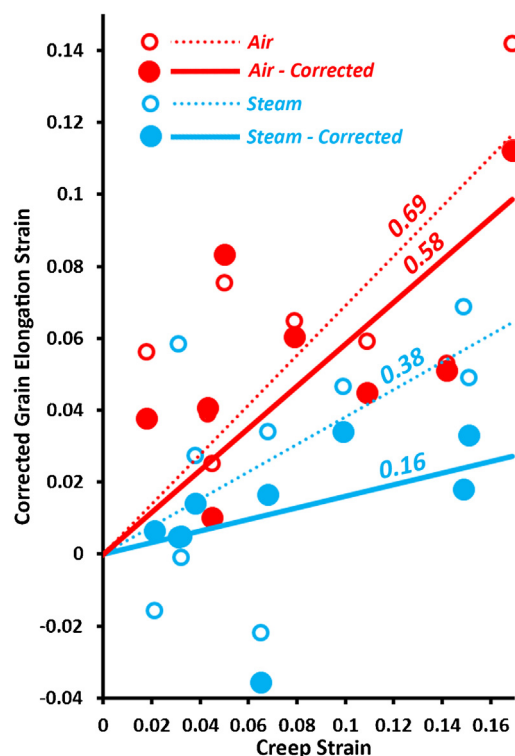


Fig. 11. Grain elongation strain vs. creep strain for Nextel™ 610 fibers after creep in air and steam at 1100 °C. The “corrected” data accounts for elongation from grain growth.

time, Q is an activation energy, and RT has the usual meaning. The best fit of Eq. (2) to all the values of X for the heat-treated fibers yields (Fig. 7):

$$X_0 = 7.6 \times 10^{-8} \text{ m} \quad (3a)$$

$$K = 2.4 \times 10^{-15} \text{ m}^m/\text{s} \quad (3b)$$

$$m = 5.2 \quad (3c)$$

$$Q = 770 \text{ kJ/mol} \quad (3d)$$

The growth exponent m is quite large; it should be 2 for normal grain growth,⁷² and there are no theoretical predictions for m values larger than 4.⁷³ However, values of m as high as 7 have been observed in alumina. They are attributed to solute drag from grain boundary segregation of impurities, with the amount of segregation increasing as grain growth reduces grain boundary area.⁷³ For Nextel™ 610 the segregant is Si. This explanation for high m contrast with that for plate-like grain growth in Nextel™ 610, which was attributed to Si depletion from grain boundaries.⁷⁰ The calculated activation energy (Q) is consistent with previously reported values that range from 700 to 800 kJ/mol, albeit with a lower growth exponent m .⁷⁴ Q of 770 kJ/mol is similar to values of Q for oxygen lattice diffusion and grain boundary diffusion of ~ 800 kJ/mol.^{47,75} The initial grain size X_0 of 76 nm is ~ 88 nm after stereological correction for equant grains. This is similar to the ~ 100 nm and 80 nm grain size reported previously.^{33,76}

The effects of steam and stress on grain growth are illustrated in Fig. 8. The three data points for heat-treated fibers in

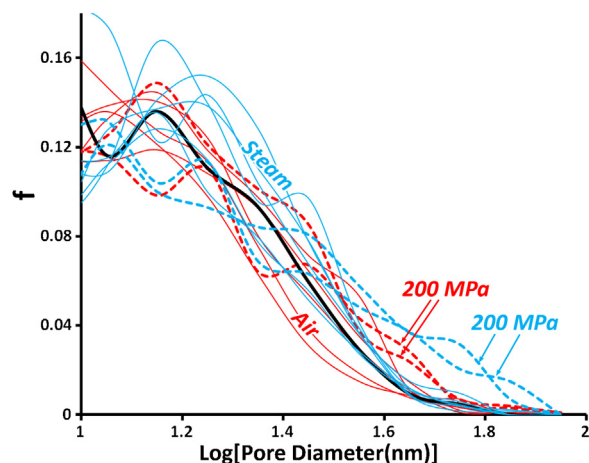


Fig. 12. Pore diameter (equivalent diameter) histograms of pores larger than 10 nm for Nextel™ 610 fibers after creep in air and steam at 1100 °C.

air are plotted as open circles, and the grain growth law calculated in Eqs. (2) and (3a)–(3d) for 1100 °C is plotted as a dashed line. Exaggerated grain growth at the fiber surface from loss of the trace silica incorporated in the Nextel™ 610 fiber as a grain growth inhibitor, as reported for temperatures above 1100 °C,^{63,70} was not observed for either air or steam creep tested fibers.²⁴ Maximum grain size at 1100 °C was $X = 93$ nm in steam and $X = 86$ nm in air, increases of 22% and 13%, respectively. This is not enough to have a significant effect on strain rates during creep, regardless of the creep mechanism. The grain size after creep in steam was consistently larger than after creep in air, and grain sizes after creep in air were slightly larger than grain sizes after heat-treatment in air without creep. This suggests that both stress and steam increase grain growth rates in alumina. Stress driven grain growth has been reported many times for nanocrystalline metals.^{77–81} Observations of effects of water on grain growth in oxides are very limited; water had only a small effect on grain growth in calcite at 900 °C.⁸²

3.2. Grain elongation along the fiber axis

Grain elongation along the fiber axis (ϵ) is the ratio of the average grain intercept length along the fiber axis to the intercept length perpendicular to the axis. It is calculated by measuring average grain intercept lengths along lines oriented at 10° increments between 0° and 90° to the fiber axis, using the same sets of digitally identified grains that were used to quantify grain growth. Grain intercept lengths for fibers from creep experiments, and for as-received fiber, are shown in Fig. 9. Grain intercept lengths do not always traverse the grain center, and therefore average $\sim 20\%$ smaller than equivalent fiber diameters (Fig. 8). The best fit to an ellipse was found for each data set, and the ratio of the major/minor ellipse axes is ϵ . The ellipse fits for grain intercept lengths are also shown in Fig. 9. Elongation calculated on a percent basis is $100(\epsilon - 1)$; this is listed in Table 1 for direct comparison with creep strain (ϵ , %).

The 100 MPa creep experiments, in both steam and air, are shown as dotted lines, and the 200 MPa creep experiments as thin lines (Fig. 9). There was more grain growth in steam (Fig. 8), so

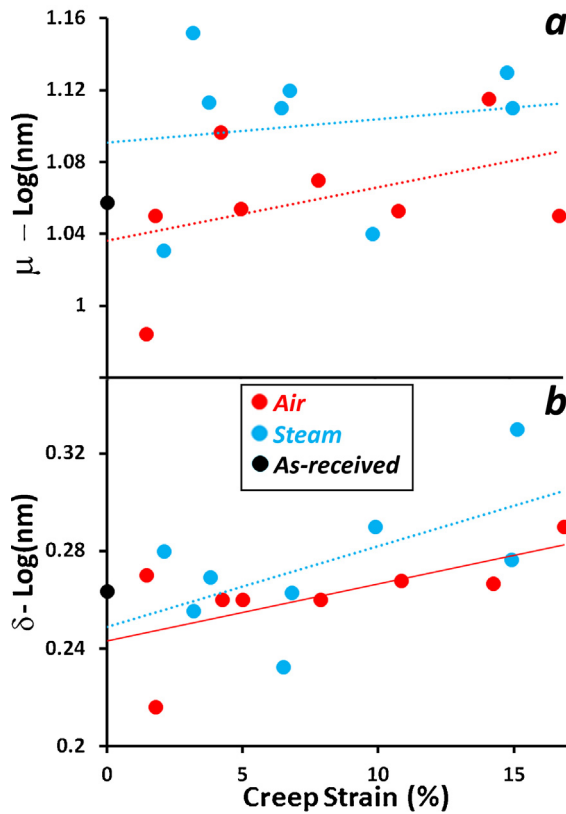


Fig. 13. (a) Log-average (μ) and (b) log-standard deviation (δ) for log-normal pore size distributions for Nextel™ 610 fibers after creep in air and steam at 1100 °C.

the grain intercept lengths for fibers from creep tests in steam were usually larger than those in air. There is pre-existing grain elongation of 12% ($\epsilon_0 = 0.12$) in the as-received fiber (Table 1). The largest grain elongations were in fibers with the most creep strain, particularly those in air (Fig. 9); the largest creep strains accumulated for the 200 MPa creep tests. Grain elongations as high as 31% (Table 1) were measured.

Grain elongation along the fiber axis (ϵ_{GG}) occurs during grain growth (Fig. 4), without any applied stress. For heat-treated fibers in air (Table 2, Fig. 7), ϵ_{GG} was determined by the same methods used for fibers from creep tests. A linear relationship between ϵ_{GG} and $\log[X]$ was found (Fig. 10):

$$1 + \epsilon_{GG} = 1.035 \log[X(m)] + 8.484 \quad (4)$$

If the contribution of grain growth to grain elongation is the same, regardless of whether grain growth occurs in steam, air, or with or without applied stress, the separate contribution of grain growth to grain elongation can be distinguished with Eq. (4). The corrected contribution of grain elongation (ϵ_C) to strain during a creep test is found by subtracting the initial grain elongation found in the fibers (ϵ_0) of 0.12, correcting for grain elongation from grain growth during creep using Eq. (4) and values for X from Table 1, and correcting for Poisson contraction during grain elongation:

$$\epsilon_C = (\epsilon - \epsilon_0 - \epsilon_{GG} + 1)^{2/3} - 1 \quad (5)$$

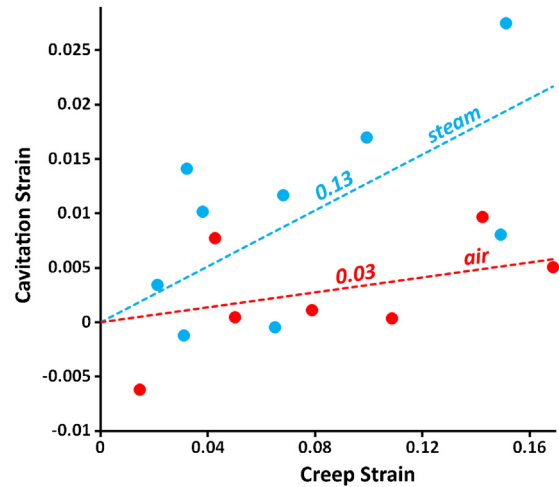


Fig. 14. Cavitation strain (ϵ_P) vs. creep strain for Nextel™ 610 fibers after creep in air and steam at 1100 °C.

Results from these calculations are plotted in Fig. 11, both with and without the grain growth correction. For creep experiments in air there is significant scatter, but average behavior illustrated by the trend-line shows that grain elongation contributed to ~58% of total creep strain. There was little grain growth in fibers that were creep tested in air, so the grain growth correction was relatively small. For creep experiments in steam there was also significant scatter, but the trend-lines show, on average, that 16% of the creep strain can be accounted for by grain elongation after correction for grain growth. There was more grain growth in fibers during creep tests in steam than in air (Fig. 8), so the grain growth corrections are relatively large.

Small grain-shape changes that occur during creep of Nextel™ 610 at 1100 °C are measurable and trends are clear, but they are difficult to quantify with great accuracy. However, firm semi-quantitative conclusions can be drawn. A significant fraction, >50%, of creep strain in air comes from elongation of individual grains, but for creep in steam a much smaller fraction, <20%, comes from grain elongation. Another possible source of creep strain during tensile tests of fibers is pore growth, which will be discussed next.

3.3. Pore growth

Pore growth was obvious in TEM micrographs of fibers that were creep tested in steam to large strains (Fig. 2). Little pore growth was evident in fibers creep tested in air to similar large strains. Pore growth in steam, but not in air, was previously observed after creep testing of Nextel™ 720 fibers, a fine-grained alumina–mullite fiber.²⁵ An increase in the pore volume fraction (ϕ) will increase the strain during creep:

$$\epsilon_P = \left[\frac{1}{1 - (\phi - \phi_0)} \right] - 1 \quad (6)$$

This (ϵ_P) is referred to as “cavitation” strain.

10 nm pores are abundant in as-received Nextel™ 610. The fiber density is 3.9, and theoretical density for α -Al₂O₃ is 3.984, which yields an initial pore volume (ϕ_0) of 2.1%. Unfortunately, the pore volume fraction cannot be easily measured from TEM

micrographs. Projected pore area increases with TEM sample thickness, which varies significantly between different images and with thickness gradients along an image, so a different method was used.

It was assumed that there was no pore nucleation during creep; the only increase in ϕ came from growth of pre-existing pores, which were already abundant. A log-normal pore size distribution (equivalent diameter) was measured for as-received fiber with 2.1% porosity (ϕ_0) and for all creep-tested fibers. These distributions are shown in Fig. 12 for pores larger than 10 nm. For creep tests with the most strain (200 MPa, Table 1) large pores were more abundant, particularly for fibers tested in steam.

The average (μ) and standard deviation (λ) were calculated for log-normal pore size distributions from data used for Fig. 12, and are plotted in Fig. 13. There is significant scatter in μ and λ , but trends are evident. μ and λ for steam were usually larger than those in air, and μ and λ increase with creep strain. The individual diameters (d_i) for each pore in an assemblage of 1000 pores, which was the typical number measured, were numerically calculated from the continuous log-normal distribution function for μ and δ for as received fibers using a MathematicaTM program. Total pore volume (V_p) was then calculated numerically for as-received fibers:

$$V_p = (1/6) \pi \sum (d_i^3) \quad [i = 1 - 1000] \quad (7)$$

A correction factor ϕ_0/V_p that normalized V_p to ϕ_0 of 2.1% was determined. The procedure was repeated for the log-normal pore-size distributions for creep tested fibers. The correction factor was used to determine ϕ for fibers from each creep test from the total pore volume calculated in Eq. (7). Note that for a log-normal distribution, ϕ is very sensitive to δ , particularly since pore diameters are cubed to determine volume; total pore volume is dominated by a relatively small number of large pores when δ is large. Computed pore volume fractions (ϕ) are listed in Table 1.

The values for cavitation strain (ϵ_p) were calculated from ϕ (Eq. (6)) and are plotted against creep strain in Fig. 14. For many creep tests a high μ and low δ , or vice versa, tend to balance each other out, so the trends for (ϵ_p) are a little clearer than those for μ and δ in Fig. 13. Creep experiments in steam have more cavitation strain, averaging about 13% of creep strain. Creep experiments in air have cavitation strains that average only about 3% of creep strain, an insignificant amount.

3.4. Creep rate comparisons

Measured NextelTM 610 steady-state creep rates ($\dot{\epsilon}$) at 1100 °C are compared with previous measurements in Fig. 1. These rates are described by the usual power laws:

$$\dot{\epsilon} \text{ (s}^{-1}\text{)} \approx 3 \times 10^{-38} \sigma^{3.7} \text{ (Pa)} \text{ (steam)} \quad (8a)$$

$$\dot{\epsilon} \text{ (s}^{-1}\text{)} \approx 3 \times 10^{-33} \sigma^{3.2} \text{ (Pa)} \text{ (air)} \quad (8b)$$

Creep rates in air were about $3 \times$ to $10 \times$ slower than those measured previously, and n of 3.7 is higher than previously reported values of 2.9 and 3.^{33,34} To the best of our knowledge

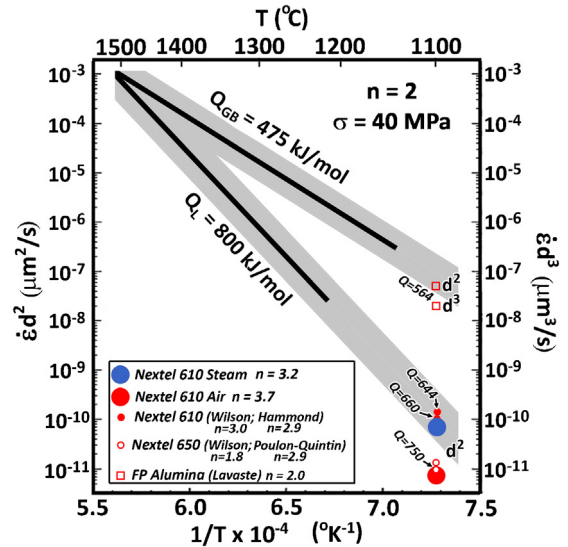


Fig. 15. Grain-size compensated alumina creep rates at $\sigma = 40$ MPa vs. reciprocal temperature (after Ruano).⁴⁷ Compressive creep rates for grain sizes $> 1 \mu\text{m}$ and $T > 1150$ °C are shown as gray bands. Measurements or measurement extrapolations for alumina fibers with grain size $\ll 1 \mu\text{m}$ are shown as separate points, and denoted in the legend.

there are no previous measurements of NextelTM 610 creep in steam. Results are also compared with NextelTM 650, an 89 wt% Al_2O_3 –10 wt% ZrO_2 –1 wt% Y_2O_3 fiber with 100 nm grain size,^{33,83} and with DuPont fiber FP, an alumina fiber with 500 nm grain size.³⁰ NextelTM 650 has slower creep rates than NextelTM 610, and lower n , measured to be 1.8 and 2.9, respectively.^{33,83} DuPont Fiber FP has creep rates one to two orders of magnitude faster than NextelTM 610, despite a much larger grain size, and n of 2.0.³⁰

There is significant variation in the creep rate measurements for the same fibers. The period in which these different measurements were made spans nearly 20 years. The filament strength of NextelTM 610 increased from 1.8 to 3.3 GPa over a 10 year interval from use of improved nucleation agents, reduction of particulate defects, and change of fiber spinning and heat-treatment parameters.³³ There will be subtle differences in fiber microstructure, composition, and grain-boundary chemistry that change with fiber vintage as it is incrementally improved. This may be responsible for at least some of the differences in measured creep rates.

The tendency for creep of fine-grained alumina to be non-Newtonian ($n > 1$), and not follow Nabarro–Herring or Coble creep flow laws often observed for very fine-grained materials, has been widely noted.^{37,47} These observations were made in compression for alumina with grain sizes between 1 and 100 μm , and at temperatures greater than 1100 °C. The grain size of NextelTM alumina fibers is $\sim 10 \times$ lower than the smallest grain sizes studied for compressive creep. Creep rates of NextelTM 610,^{23,24,33,34} NextelTM 650,^{33,83} and DuPont Fiber FP³⁰ are compared with creep rates measured for coarse grained alumina in compression, following the methods and using the data from 35 different creep studies reviewed by Ruano et al. (Fig. 15).⁴⁷ Creep rates were normalized for grain size using d^2

for Nextel™ 610 ($d = 100$ nm) and Nextel™ 650 ($d = 100$ nm), and using both d^2 and d^3 for DuPont Fiber FP ($d = 500$ nm). The creep rates for an applied stress of 40 MPa are shown. These were extrapolated from measured flow stress exponents (Eqs. (8a) and (8b)) if creep measurements were not actually made at that stress.

Data for grain-size compensated compressive creep rates of alumina tends to be in two bands.⁴⁷ These are shown by black lines surrounded by a gray band in Fig. 15, and are extrapolated to <1100 °C. A band with $n = 2$ and $Q \approx 800$ kJ/mol, and another band with $n = 2$ and $Q \approx 475$ kJ/mol correspond to mechanisms of grain-boundary sliding (GBS) accommodated by dislocation climb governed by lattice and grain-boundary diffusion of oxygen, respectively. It should be noted that these mechanistic interpretations are controversial; for example, tensile creep in fine-grained alumina with $n = 2.2$ and Q of 492 kJ/mol has been attributed to GBS accommodated by dislocation climb limited by aluminum lattice diffusion.⁸⁴ The assumptions concerning Q for lattice and grain boundary diffusion are also very controversial. A recent review states that ~ 530 kJ/mol $< Q_L < \sim 675$ kJ/mol for oxygen, suggests that Q_{GB} may be larger than Q_L , and notes that there are no studies that determine whether Al grain boundary diffusion is slower or faster than O grain boundary diffusion.⁷⁵

Creep of DuPont Fiber FP has $n = 2$ and grain-size compensated creep rates clearly fall near the $Q = 475$ kJ/mol band. An activation energy of ~ 560 kJ/mol was calculated from creep rates measured for this fiber.³⁰

Although measured n for the more fine-grained Nextel™ fibers range from 1.8 to 3.7, and despite uncertainty in Q , measured or extrapolated grain-size compensated creep rates fall near the $Q_L = 800$ kJ/mol band. Activation energies of 644 and 660 kJ/mol were calculated for Nextel™ 610,^{28,33,85} and Q of ~ 750 kJ/mol was found for Nextel™ 650,⁸³ which are in better accord with the lower reported Q_L values.⁷⁵ Implications for Nextel™ 610 creep mechanisms, along with the implications from microstructural observations, are discussed for both steam and air.

3.5. Creep mechanisms

3.5.1. General

Microstructural observations for Nextel™ 610 after creep at 1100 °C can be semi-quantitatively summarized as follows:

1. Grain elongation accounts for a large fraction, probably greater than 50%, of the creep strain during creep in air, but grain elongation is much less pronounced in steam.
2. There is significant pore growth (cavitation strain) during creep in steam, but cavitation strain can account for only 10–20% of the creep strain. There is almost no pore growth during creep in air.
3. There is more grain growth in steam than in air, but grain size increased by no more than $\sim 25\%$ after 100 h in steam at 1100 °C. Grain elongation along the fiber axis in steam is mostly due to grain growth in steam.

3.5.2. Steam

The retention of equiaxed grain structure after creep in steam is consistent with mechanisms dominated by grain boundary sliding,^{47,86,87} specifically a Racherer GBS mechanism accommodated, and rate limited, by dislocation climb governed by lattice diffusion rates.⁸⁷ Flow stress exponents of $n = 2$ and $n = 3$ are possible, depending on whether the grain size (d) is smaller or larger than the equilibrium subgrain size (λ), respectively⁸⁷:

$$\dot{\epsilon} = \left(\frac{A' D_{GB} G b}{kT} \right) \left(\frac{b}{d} \right)^2 \left(\frac{\sigma}{G} \right)^2 \quad d < \lambda \quad (9a)$$

$$\dot{\epsilon} = \left(\frac{A'' D_L G b}{kT} \right) \left(\frac{b}{d} \right) \left(\frac{\sigma}{G} \right)^3 \quad d < \lambda \quad (9b)$$

where A' and A'' are constants, D_{GB} is the boundary diffusion coefficient and D_L the lattice diffusion coefficient, G is the shear modulus and b the Burgers vector magnitude, and kT has the usual meaning.

The model of Ruano et al. (Fig. 15) is slightly different⁴⁷:

$$\dot{\epsilon} = \left(\frac{A' D_{eff}}{d^2} \right) \left(\frac{\sigma}{E} \right)^2 \quad (10a)$$

$$D_{eff} = D_L + c\pi \left(\frac{b}{d} \right) D_{GB} \quad (10b)$$

where E is Young's modulus and c is a constant. There are no conditions where $n = 3$.

There are several models for the equilibrium subgrain size (λ). The models for a $1/d^2$ dependence on grain size are^{88–92}:

$$\lambda = K_1 \sigma^{-1} \quad (11a)$$

$$\lambda = K_2 \sigma^{-n} \quad (1.3 \leq n \leq 1.5) \quad (11b)$$

$$\lambda = K_3 \sigma^{-n/4} \exp \left[\frac{Q_C - Q_{Cl}}{4RT} \right] \quad (11c)$$

$$\lambda = K_4 \sigma^{-n/2} \exp \left[\frac{Q_L - Q_{GB}}{2RT} \right] \quad (11d)$$

$$\lambda = K_5 \sigma^{-1.25} \exp \left[\frac{Q_L - Q_{GB}}{4RT} \right] \quad (11e)$$

$$\lambda = K_6 \sigma^{-(n-1)/2} \exp \left[\frac{Q_C - Q_L}{2RT} \right] \quad (11f)$$

where K_{1-6} are constants, Q_C is the activation energy for creep, Q_{Cl} for dislocation climb, Q_L for lattice diffusion, and Q_{GB} for grain boundary diffusion. Q_{Cl} in general will equal Q_L , and the evidence suggests that either $Q_C \approx Q_L$,⁷⁵ or Q_C is slightly lower than Q_L for Nextel™ 610 (Fig. 15).⁴⁷ Therefore there is either little no temperature dependence of λ (11a) and (11b), possibly a decrease with increasing T (11c) and (11f), or either a large increase or decrease with decreasing T (11d) and (11e), depending on which values of Q_L (530–800 kJ/mol) and Q_{GB} (475–800 kJ/mol) are used. No firm conclusions about temperature dependence of λ can be drawn. A comprehensive comparison of these models to existing data in a wide variety of materials favored (11f).⁸⁸ High σ of up to 0.5 GPa for our Nextel™ 610 experiments clearly promotes low λ in all cases,

but subgrains were not observed by TEM inside the ~ 100 nm grains after creep (Fig. 2). Flow stress exponents n are clearly >2 (Fig. 1); we suggest that Eq. (9b) must therefore apply, despite lack of subgrain observation. The fiber grain size is so small that the subgrains may coarsen to the grain size in the short time the fibers see temperature without load after failure before they are extracted from the furnace. Another possibility is that silica doping inhibits grain boundary diffusion rates and raises boundary diffusion activation energies to such an extent that lattice diffusion at the low temperature of 1100°C is the more rapid transport process, and Eq. (9b) applies regardless of λ values. Boundary diffusion inhibition has been suggested for Y, La, and Lu doping in Al_2O_3 .^{47,75,93} It is also conceivable that water enhances lattice diffusion more than grain boundary diffusion, further promoting the $n=3$ mechanism in Eq. (9b). The $d>\lambda$ mechanism implies little temperature dependence for λ in these low temperature experiments; creep and recovery would both be controlled by oxygen lattice diffusion. As σ decreases below 100 MPa the $d<\lambda$ condition with $n=2$ (9a) should eventually apply; we speculate that this may occur around $\sigma=40$ MPa, which could explain why the extrapolated grain-size compensated creep rates are consistent with $Q_L=800$ kJ/mol in the model of Ruano et al. (Fig. 15).⁴⁷

3.5.3. Air

The grain elongation that occurs during creep in air is not consistent with predominance of a grain boundary sliding mechanism, although there may still be a small sliding component to the deformation. The various observations of flow stress exponents range from $n=2.9$ to $n=3.7$. Some mechanism other than GBS, with $2.5<n<4.0$, is rate-limiting for NextelTM 610 creep at 1100°C in air. Previous studies of temperature dependence suggest Q for this mechanism is ~ 650 kJ/mol,^{28,33,34} similar to some recent estimates of Q for oxygen lattice diffusion.⁷⁵ Comprehensive reviews of creep in ceramics conclude that $n=3$ mechanisms result from climb of dislocations from Bardeen Herring sources under conditions where there are not 5 independent and interpenetrating slip systems.^{94,95} The simplest conclusion for creep mechanisms in air is that the rate-limiting mechanism, dislocation slip rate limited by dislocation climb, is not only rate limiting as it is in steam, but also dominates the elongation.

For NextelTM 650, Q of 750 kJ/mol and n of 1.8 to 2.9 are more consistent with GBS accommodation by dislocation climb controlled by oxygen lattice diffusion by either Eq. (9a) or Eq. (9b) (Fig. 15). Unfortunately detailed microstructural observations that include grain elongation measurement are lacking. For DuPont Fiber FP, flow stress exponents and grain-size compensated creep rates are consistent with GBS accommodation by dislocation climb controlled by oxygen grain boundary diffusion (Fig. 15). Reported Q of 560 kJ/mol is somewhat higher than values for oxygen grain boundary diffusion used by Ruano et al.,⁴⁷ but lower than many values of ~ 800 kJ/mol discussed in a recent review.⁷⁵ We speculate that grain-boundary diffusion control is due to an intergranular film derived from grinding contaminants and sintering additives used to make this fiber, and the low values used by Ruano et al. apply to ceramics with

relatively thick intergranular films. Higher values for Q_{GB} are for boundaries that lack these films.

3.5.4. Cavitation

Cavitation has previously been observed during creep of polycrystalline alumina in flexure,^{38,96} and in tension.⁹⁷ As in NextelTM 610, cavitation strain did not significantly contribute to creep strain. Analysis of the cavitation rates suggested that it did not contribute to the non-linearity of flow rates.⁹⁶ Pore growth in steam, but not in air, during fiber creep was also observed for NextelTM 720 fiber when large creep strains accumulated.²⁵ This is an α -alumina–mullite fiber with 57:43 volume ratio, with 63 nm plate-like alumina grains dispersed in 230 nm equiaxed mullite grains.^{25,53} Creep rates of these fibers in steam were an order of magnitude higher than those in air at stresses <300 MPa, similar to NextelTM 610 (Fig. 1),²⁴ but there was no effect when stress exceeded 300 MPa at 1200°C . The flow stress exponent was $n\approx 3$ at 1100°C in air and in steam for σ from 100 to 400 MPa, which is also similar to NextelTM 610. At 1200°C in air and in steam, n changed from $n\approx 3$ to $n\approx 5$ as σ exceeded 300 MPa. It was suggested that climb-controlled dislocation recovery operates at 100–300 MPa, with transition to a mechanism above 300 MPa where five independent and interpenetrating slip systems are activated, rather than three.^{94,95} Because of the very small grain sizes, climb is controlled by grain boundary diffusion, which is increased by hydroxyl groups and/or hydrogen from steam. The additional slip systems activated at high stress were evidently not affected by steam. Cavitation during creep in steam was consistent with effects of increased grain boundary diffusion in cavitation models.^{25,98,99} The cavitation observed in NextelTM 610 in steam, but not in air, is also consistent with increased grain boundary diffusion rates in steam (Figs. 2 and 14). As discussed in Section 3.5.2, both grain boundary diffusion and lattice diffusion may be enhanced in steam, but the relative effect of steam may be greater for lattice diffusion.

3.5.5. Discussion

For creep of NextelTM 610 in steam at 1100°C and 100–500 MPa, the most plausible creep mechanism is grain boundary sliding, with accommodation of compatibility strains by dislocation slip rate limited by climb with $n\sim 3$ (9b). Cavitation may accommodate some of sliding, but is not a rate limiting mechanism. It does not contribute enough strain and is inconsistent with non-Newtonian creep rates,⁹⁶ and is a byproduct of higher grain boundary diffusion rates in steam. Creep of NextelTM 610 in air at 1100°C and 100–500 MPa, the most plausible creep mechanism is also the rate-limiting mechanism, which is dislocation slip rate limited by climb with $n\sim 3$ (9b). A small amount on GBS may occur, but it does not dominate deformation. For both air and steam, creep should transition to an $n=2$ mechanism (9a) and (10a) at lower stresses. The temperature dependence is problematic.

The postulated rate-limiting mechanism is the same for both steam and air, but there was a $\sim 10\times$ increase in creep rates in steam (Fig. 1). A previous study at high hydrostatic pressure (1.5–2 GPa) of 3–5 μm grain size Al_2O_3 at 700–730 $^\circ\text{C}$ and with

σ of ~ 0.5 – 3.5 GPa found a $6\times$ increase in creep rate for water saturated samples.⁴⁹ This was attributed to GBS. Intragranular dislocations were not observed by TEM, despite the higher σ and larger d in these experiments which would suggest the $d > \lambda$ condition for Eq. (9b) applies. An analysis of the rate limiting mechanism for GBS was not presented. A $2\times$ increase found for water saturated Al_2O_3 single crystals was attributed to changes in dislocation glide. For NextelTM 610, the simplest conclusion is that water increases D_L , which for $n=3$ mechanisms increase creep rates that are rate-limited by dislocation climb modeled in Eq. (9b). Cavitation in steam, but not in air, suggests that water also increases D_{GB} , as suggested for NextelTM 720 alumina–mullite fiber,²⁵ and would increase creep rates rate-limited by dislocation climb modeled by Eqs. (9a) and/or (10a) and also contribute to early failure by creep-rupture²⁴.

4. Summary and conclusions

Small microstructural changes during creep of NextelTM 610 in steam and air at 100–500 MPa at 1100 °C were quantified by TEM and image analysis. These creep rates were:

$$\dot{\epsilon} \text{ (s}^{-1}\text{)} \approx 3 \times 10^{-38} \sigma^{3.7} \text{ (Pa)} \text{ (steam)}$$

$$\dot{\epsilon} \text{ (s}^{-1}\text{)} \approx 3 \times 10^{-33} \sigma^{3.2} \text{ (Pa)} \text{ (air)}$$

At 100–500 MPa, creep rates were $\sim 10\times$ faster in steam than in air. These results, along with some previous measurements of fiber creep, extend a large body of work on creep in alumina to much smaller grain sizes and lower temperatures.

To separate the effects of stress and temperature on microstructural evolution, grain growth and elongation were also quantified for fibers heat-treated for 1–100 h in air at 1100–1500 °C. There is significant scatter in individual results, but trends are consistent and clear in a semi-quantitative sense. Grain growth formed plate-like grains with a $[1\ 1\ 1]_{\text{rho}}$ axis (short axis) that tended to be oriented perpendicular to the fiber axis. Grain growth therefore caused some grain elongation along the fiber axis. Standard deviations of log-normal grain size distributions increased with grain size in a continuous manner. There was no clear grain size at which normal grain growth transitioned to abnormal grain growth. Grain growth kinetics for the inverse log-average of the equivalent grain diameter (\bar{X}), uncorrected by stereological analysis, best fit the expression:

$$\bar{X}(\text{m})^{5.2} - (7.6 \times 10^{-8})^{5.2} = 2.4 \times 10^{-15} \text{ (m}^{5.2}\text{/s)} t(\text{s}) \\ \times \exp\left(\frac{-770,000}{RT}\right)$$

This is a crude approximation to the highly anisotropic grain shapes found at 1300 °C and higher, but is a reasonable for the nearly equiaxed shapes found at ≤ 1200 °C. Grain elongation along the fiber-axis during grain growth (ϵ_{GG}) was described by:

$$1 + \epsilon_{\text{GG}} = 1.035 \log[\bar{X}(\text{m})] + 8.484$$

Grain elongation along the fiber axis of 12% was present in the as-received fibers. There was significantly more grain growth in steam than in air, but grain sizes did not increase by more than 25% in 100 h. When grain elongation was corrected for grain growth during creep, grain elongation along the fiber axis accounted for $>50\%$ of the creep strain in air, and $<20\%$ in steam. Cavitation strain accounted for $<5\%$ of the creep strain in air, and $<20\%$ in steam. Increased cavitation in steam is a byproduct of increased grain boundary diffusion coefficients in steam. Cavitation may relieve some compatibility strain during grain boundary sliding, but it is not expected to be rate-limiting.

Retention of an equiaxed grain microstructure in steam during creep was consistent with a grain boundary sliding mechanism. Creep rate measurements and microstructural characterization suggest that grain boundary sliding accommodated by dislocation slip that was rate-limited by climb, called Rachinger sliding with $n \approx 3$, is the most plausible creep mechanism for NextelTM 610 at 100–500 MPa at 1100 °C in steam. Dislocation slip rate-limited by climb is tentatively suggested to be both the dominant deformation mechanism and the rate-limiting mechanism for creep in air. Both steam and air are suggested to have the same rate-limiting mechanism, but rates are increased in steam by increased lattice diffusion coefficients. As stress decreases, these mechanisms are expected to transition to a mechanism rate-limited by grain boundary diffusion, with $n \approx 2$, which will also be enhanced in steam. Future work to better define these mechanisms requires more precise and reproducible measurement of creep, lattice, and grain boundary diffusion rates and activation energies, flow stress exponents, and microstructural changes, and the effect of various dopants such as SiO_2 or rare earth oxides on these phenomenon.

References

1. Zok FW. Developments in oxide fiber composites. *J Am Ceram Soc* 2006;**89**:3309–24.
2. Kerans RJ, Hay RS, Parthasarathy TA, Cinibulk MK. Interface design for oxidation resistant ceramic composites. *J Am Ceram Soc* 2002;**85**:2599–632.
3. Yang JY, Weaver JH, Zok FW, Mack JJ. Processing of oxide composites with three-dimensional fiber architectures. *J Am Ceram Soc* 2009;**92**:1087–92.
4. Kanka B, Schneider H. Aluminosilicate fiber/mullite matrix composites with favorable high-temperature properties. *J Eur Ceram Soc* 2000;**20**:619–23.
5. Carelli EAV, Fujita H, Yang JY, Zok FW. Effects of thermal aging on the mechanical properties of a porous-matrix composite. *J Am Ceram Soc* 2002;**85**:595–602.
6. Mattoni MA, Yang JY, Levi CG, Zok FW, Zawada LP. Effects of combustor rig exposure on a porous-matrix oxide composite. *Int J Appl Ceram Technol* 2000;**2**:133–40.
7. Staehler JM, Zawada LP. Performance of four ceramic-matrix composite divergent flap inserts following ground testing on an F110 turbofan engine. *J Am Ceram Soc* 2000;**83**:1727–38.
8. Hackemann S, Flucht F, Braue W. Creep investigations of alumina-based all-oxide ceramic matrix composites. *Composites A* 2010;**41**:1768–76.
9. Keller KA, et al. Effectiveness of monazite coatings in oxide/oxide composites after long term exposure at high temperature. *J Am Ceram Soc* 2003;**86**:325–32.
10. Zawada LP, Hay RS, Staehler J, Lee SS. Characterization and high temperature mechanical behavior of an oxide/oxide composite. *J Am Ceram Soc* 2003;**86**:981–90.

11. DiCarlo JA, Yun HM. Creep of ceramic fibers: mechanisms, models, and composite implications. In: Mishra RS, Earthman JC, Raj SV, editors. *Creep deformation: fundamentals and applications*. Warrendale, PA: The Minerals, Metals, and Materials Society; 2002. p. 195–208.
12. DiCarlo JA. Creep limitations of current polycrystalline ceramic fibers. *Compos Sci Technol* 1994;**51**:213–22.
13. Mehrman JM, Ruggles-Wrenn MB, Baek SS. Influence of hold times on the elevated-temperature fatigue behavior of an oxide–oxide ceramic composite in air and in steam. *Compos Sci Technol* 2007;**67**:1425–38.
14. Ruggles-Wrenn M, Braun J. Effects of steam environment on creep behavior of Nextel™ 720 alumina ceramic composite at elevated temperature. *Mater Sci Eng A* 2008;**497**:101–10.
15. Ruggles-Wrenn MB, Genelin CL. Creep of Nextel™ 720/alumina–mullite ceramic composite at 1200 °C in air, argon, and steam. *Compos Sci Technol* 2009;**69**:663–9.
16. Ruggles-Wrenn MB, Koutsoukos P, Baek SS. Effects of environment on creep behavior of two oxide/oxide ceramic-matrix composites at 1200 °C. *J Mater Sci* 2008;**43**:6734–46.
17. Ruggles-Wrenn MB, Kutsal T. Effects of steam environment on creep behavior of Nextel™ 720/alumina–mullite ceramic composite at elevated temperature. *Composites A* 2010;**41**:1807–16.
18. Ruggles-Wrenn MB, Ozer M. Creep behavior of Nextel™ 720/alumina–mullite ceramic composite with $\pm 45^\circ$ fiber orientation at 1200 °C. *Mater Sci Eng A* 2010;**527**:5326–34.
19. Ruggles-Wrenn MB, Laffey PD. Creep behavior of Nextel™ 720/alumina ceramic composite at elevated temperature in air and in steam. *Compos Sci Technol* 2008;**68**:2260–6.
20. Ruggles-Wrenn MB, Siegert GT, Baek SS. Creep behavior of Nextel™ 720/alumina ceramic composite with $\pm 45^\circ$ fiber orientation at 1200 °C. *Compos Sci Technol* 2008;**68**:1588–95.
21. Ruggles-Wrenn MB, Szymczak NR. Effects of steam environment on compressive creep behavior of Nextel™ 720/alumina ceramic composite at 1200 °C. *Composites A* 2008;**39**:1829–37.
22. Ruggles-Wrenn MB, Yeleser T, Fair GE, Davis JB. Effects of steam environment on creep behavior of Nextel 610/monazite/alumina composite at 1100 °C. *Appl Comput Mater* 2009;**16**:379–92.
23. Armani CJ [Ph.D. thesis] *Creep performance of oxide ceramic fiber materials at elevated temperature in air and in steam*. Air Force Institute of Technology; 2011.
24. Armani CJ, Ruggles-Wrenn MB, Fair GE, Hay RS. Creep of Nextel™ 610 fiber at 1100 °C in air and steam. *Int J Appl Ceram Technol* 2013;**10**:276–84.
25. Armani CJ, Ruggles-Wrenn MB, Hay RS, Fair GE. Creep and microstructure of Nextel™ 720 fiber at elevated temperature in air and steam. *Acta Mater* 2013;**61**:6114–24.
26. Pysher DJ, Tressler RE. Tensile creep rupture behavior of alumina-based polycrystalline oxide fibers. *Ceram Eng Sci Proc* 1992;**13**:218–26.
27. Pysher DJ, Tressler RE. Creep rupture studies of two alumina-based ceramic fibers. *J Mater Sci* 1992;**27**:423–8.
28. Wilson DM, Lunenburg DC, Lieder SL. High temperature properties of Nextel 610 and alumina-based nanocomposite fibers. *Ceram Eng Sci Proc* 1993;**14**:609–21.
29. Wilson DM, Lieder SL, Lunenburg DC. Microstructure and high temperature properties of Nextel 720 fibers. *Ceram Eng Sci Proc* 1995;**16**:1005–14.
30. Lavaste V, Besson J, Berger M-H, Bunsell AR. Elastic and creep properties of alumina-based single fibers. *J Am Ceram Soc* 1995;**78**:3081–7.
31. Lavaste V, Berger MH, Bunsell AR, Besson J. Microstructure and mechanical characteristics of alpha-alumina-based fibres. *J Mater Sci* 1995;**30**:4215–25.
32. Goldsby JC, Yun HM, Morscher GN, DiCarlo JA. Annealing effects on creep of polycrystalline alumina-based fibers. *Mater Sci Eng A* 1998;**242**:278–83.
33. Wilson DM, Visser LR. High performance oxide fibers for metal and ceramic composites. *Composites A* 2001;**A32**:1143–53.
34. Hammond VH, Elzey DM. Comparing the creep response of alumina tows and single filaments. *Scripta Mater* 2002;**46**:287–91.
35. Crosby A, Evans PE. Creep in pure and two phase nickel-doped alumina. *J Mater Sci* 1973;**8**:1573–80.
36. Lessing PA, Gordon RS. Creep of polycrystalline alumina, pure and doped with transition metal impurities. *J Mater Sci* 1977;**12**:2291–302.
37. Cannon RM, Rhodes WH, Heuer AH. Plastic deformation of fine-grained alumina (Al_2O_3): I. Interface-controlled diffusional creep. *J Am Ceram Soc* 1980;**63**:46–58.
38. Heuer AH, Tighe NJ, Cannon RM. Plastic deformation of fine-grained alumina (Al_2O_3): II. Basal slip and nonaccommodated grain-boundary sliding. *J Am Ceram Soc* 1980;**63**:47–54.
39. Cannon WR. In: Kingery WD, editor. *Structure and properties of MgO and Al_2O_3 ceramics*. 2012. p. 741 [Am Ceram Soc; 1984, Columbus, OH].
40. Venkatachari KR, Raj R. Superplastic flow in fine-grained alumina. *J Am Ceram Soc* 1986;**69**:135–8.
41. Xue LA, Chen I-W. Deformation and grain growth of low-temperature-sintered high-purity alumina. *J Am Ceram Soc* 1990;**73**:3518–21.
42. Robertson AG, Wilkinson DS, Caceres CH. Creep and creep fracture in hot-pressed alumina. *J Am Ceram Soc* 1991;**74**:915–21.
43. French JD, Zhao J, Harmer MP, Chan HM, Miller GA. Creep of duplex microstructures. *J Am Ceram Soc* 1994;**77**:2857–65.
44. Munro RG. Evaluated material properties for a sintered A – alumina. *J Am Ceram Soc* 1997;**80**:1919–28.
45. Li Y, et al. Codoping of alumina to enhance creep resistance. *J Am Ceram Soc* 1999;**82**:1497–504.
46. Wang CM, Cargill GS, Harmer MP, Chan HM, Cho J. Atomic structural environment of grain boundary segregated Y and Zr in creep resistant alumina from EXAFS. *Acta Mater* 1999;**47**:3411–22.
47. Ruano OA, Wadsworth J, Sherby OD. Deformation of fine-grained alumina by grain boundary sliding accommodated by slip. *Acta Mater* 2003;**51**:3617–34.
48. Bataille A, Addad A, Crampon J, Duclos R. Deformation behavior of iron-doped alumina. *J Eur Ceram Soc* 2005;**25**:857–62.
49. Castaing J, Kronenberg AK, Mitchell TE, Kirby SH. Hydrogen defects in Al_2O_3 and water weakening of sapphire and alumina ceramics between 600 and 1000 °C – II. Mechanical properties. *Acta Mater* 2000;**48**:1495–504.
50. Harada Y, Suzuki T, Hirano K, Waku Y. Influence of moisture on ultra-high-temperature tensile creep behavior of in situ single-crystal oxide ceramic alumina/yttrium aluminum garnet eutectic composite. *J Am Ceram Soc* 2003;**86**:951–8.
51. Kronenberg AK, Castaing J, Mitchell TE, Kirby SH. Hydrogen defects in Al_2O_3 and water weakening of sapphire and alumina ceramics between 600 and 1000 °C – I. Infrared characterization of defects. *Acta Mater* 2000;**48**:1481–94.
52. Kohlstedt DL. The role of water in high temperature rock deformation. In: Keppeler H, Smyth JR, editors. *Water in nominally anhydrous minerals*, vol. 62. Chantilly, VA: MSA; 2006. p. 377–96.
53. Hay RS, et al. Grain growth and tensile strength of 3M Nextel 720 after thermal exposure. *Ceram Eng Sci Proc* 1999;**20**:153–63.
54. Wilson DM. Statistical tensile strength of Nextel 610 and Nextel 720 fibres. *J Mater Sci* 1997;**32**:2535–42.
55. Berger MH, Lavaste V, Bunsell AR. Properties and microstructure of small-diameter alumina-based fibers. In: Bunsell AR, Berger MH, editors. *Fine ceramic fibers*. New York, NY: Marcel Dekker; 1999. p. 111–64.
56. Bunsell AR, Berger MH. Fine diameter ceramic fibres. *J Eur Ceram Soc* 2000;**20**:2249–60.
57. Morrell RM. A tensile creep-testing apparatus for ceramic materials using simple knife-edge universal joints. *J Phys E Sci Instrum* 1972;**5**:465–7.
58. Kandil FA, Dyson BF. Tensile creep of ceramics: the development of a testing facility. *Int J High Technol Ceram* 1988;**4**:243–62.
59. DiCarlo JA. Property goals and test methods for high temperature ceramic fibre reinforcement. *Ceram Int* 1997;**23**:283–9.
60. Opila E. Influence of alumina reaction tube impurities on the oxidation of chemically-vapor-deposited silicon carbide. *J Am Ceram Soc* 1995;**78**:1107–10.
61. Cinibulk MK, Welch JR, Hay RS. Preparation of thin sections of coated fibers for characterization by transmission electron microscopy. *J Am Ceram Soc* 1996;**79**:2481–4.
62. Hay RS, Welch JR, Cinibulk MK. TEM specimen preparation and characterization of ceramic coatings on fiber tows. *Thin Solid Films* 1997;**308–309**:389–92.

63. Schmücker M, Mechnich P. Improving the microstructural stability of Nextel™ 610 alumina fibers embedded in a porous alumina matrix. *J Am Ceram Soc* 2010;**93**:1888–90.
64. Dillon SJ, Harmer MP, Rohrer GS. The relative energies of normally and abnormally growing grain boundaries in alumina displaying different complexions. *J Am Ceram Soc* 2010;**93**:1796–802.
65. Dillon SJ, Harmer MP. Relating grain boundary complexion to grain boundary kinetics II: silica-doped alumina. *J Am Ceram Soc* 2008;**91**:2314–20.
66. Jung J, Baik S. Abnormal grain growth of alumina: CaO effect. *J Am Ceram Soc* 2003;**86**:644–9.
67. Kwon OS, et al. Microstructural evolution during sintering of TiO₂/SiO₂-doped alumina: mechanism of anisotropic abnormal grain growth. *Acta Mater* 2002;**50**:4865–72.
68. Song H, Coble RL. Origin and growth kinetics of platelike abnormal grains in liquid-phase-sintered alumina. *J Am Ceram Soc* 1990;**73**:2077–85.
69. Tartaj J, Messing GL. Anisotropic grain growth in α -Fe₂O₃-doped alumina. *J Eur Ceram Soc* 1997;**17**:719–25.
70. Schmücker M, Mechnich P. Microstructural coarsening of Nextel™ 610 fibers embedded in alumina-based matrices. *J Am Ceram Soc* 2008;**91**:1306–8.
71. Venkataraman KS, DeMilia RA. Predicting the grain-size distributions in high-density, high purity alumina ceramics. *J Am Ceram Soc* 1989;**72**:33–9.
72. Martin JW, Doherty RD, Cantor B. *Stability of microstructure in metallic systems*. 2nd ed. Cambridge, UK: University Press; 1997.
73. Dillon SJ, Behera SK, Harmer MP. An experimentally quantifiable solute drag factor. *Acta Mater* 2008;**56**:1374–9.
74. Heintz JM, Bihl JC, Silvain JF. Experimental and numerical study of grain growth in alumina fibres heat treated at 1700°C. *J Eur Ceram Soc* 1999;**19**:1759–67.
75. Heuer AH. Oxygen and aluminum diffusion in α -Al₂O₃: how much do we really understand? *J Eur Ceram Soc* 2008;**28**:1495–507.
76. Xu ZR, Chawla KK, Li X. Effect of high temperature exposure on the tensile strength of alumina fiber Nextel 610. *Mater Sci Eng A* 1993;**171**:249–56.
77. Zhang Y, Sharon JA, Hu GL, Ramesh KT, Hemker KJ. Stress-driven grain growth in ultrafine grained Mg thin film. *Scripta Mater* 2013;**68**:424–7.
78. Sharon JA, Su PC, Prinz FB, Hemker KJ. Stress-driven grain growth in nanocrystalline Pt thin films. *Scripta Mater* 2011;**64**:25–8.
79. Rupert TJ, Gianola DS, Gan Y, Hemker KJ. Experimental observations of stress-driven grain boundary migration. *Science* 2009;**326**:1686–90.
80. Legros M, Gianola DS, Hemker KJ. In situ TEM observations of fast grain-boundary motion in stressed nanocrystalline aluminum films. *Acta Mater* 2008;**56**:3380–93.
81. Gianola DS, et al. Stress-assisted discontinuous grain growth and its effect on the deformation behavior of nanocrystalline aluminum thin films. *Acta Mater* 2006;**54**:2253–63.
82. Bresser JHPD, Urai JL, Olgaard DL. Effect of water on the strength and microstructure of carrara marble axially compressed at high temperature. *J Struct Geol* 2005;**27**:265–81.
83. Poulon-Quintin A, Berger MH, Bunsell AR. Mechanical and microstructural characterization of Nextel 650 alumina–zirconia fibres. *J Eur Ceram Soc* 2004;**24**:2769–83.
84. Campbell I, Fahmy Y, Conrad H. Plastic deformation kinetics of fine-grained alumina. *Metall Mater Trans* 1999;**30A**:2809–15.
85. Hammond VH [Ph.D. thesis] *Creep rupture of an oxide/oxide composite fiber*. University of Virginia; 2001.
86. Raj R, Lange FF. On the retention of equiaxed grain structure after superplastic and other forms of high temperature deformation. *Acta Metall* 1985;**33**:699–703.
87. Langdon TG. Grain boundary sliding revisited: developments in sliding over four decades. *J Mater Sci* 2006;**41**:597–609.
88. Bresser JHPD, Heege JHT, Spiers CJ. Grain size reduction by dynamic recrystallization: can it result in major rheological weakening? *Int J Earth Sci* 2001;**90**:28–45.
89. Derby B, Ashby MF. On dynamic recrystallization. *Scripta Metall* 1987;**21**:879–84.
90. Edward GH, Etheridge MA, Hobbs BE. On the stress dependence of subgrain size. *Text Microstruct* 1982;**5**:127–52.
91. Shimizu I. Stress and temperature dependence of recrystallized grain size: a subgrain misorientation model. *Geophys Res Lett* 1998;**25**:4237–40.
92. Shimizu I. Steady state grain size in dynamic recrystallization. In: Sztwiertnia K, editor. *Recrystallization*. InTech; 2012. p. 464 [chapter 15], Open access - Available from <http://intechopen.com/books>.
93. Yoshida H, Ikuhara Y, Sakuma T. High-temperature creep resistance in rare-earth-doped, fine-grained Al₂O₃. *J Mater Res* 1998;**13**:2597–601.
94. Cannon WR, Langdon TG. Review: creep of ceramics. Part II. An examination of flow mechanisms. *J Mater Sci* 1988;**23**:1–20.
95. Chokshi AH, Langdon TG. Characteristics of creep deformation in ceramics. *Mater Sci Technol* 1991;**7**:577–84.
96. Porter JR, Blumenthal W, Evans AG. Creep fracture in ceramic polycrystals – I. Creep cavitation effects in polycrystalline alumina. *Acta Metall* 1981;**29**:1899–906.
97. Kottada RS, Chokshi AH. The high temperature tensile and compressive deformation characteristics of magnesia doped alumina. *Acta Mater* 2000;**48**:3905–15.
98. Hull D, Rimmer DE. The growth of grain-boundary voids under stress. *Philos Mag* 1959;**4**:673–87.
99. Raj R, Ashby MF. Intergranular fracture at elevated temperature. *Acta Metall* 1975;**23**:653–66.